Published in final edited form as:
J Vasc Interv Radiol. 2014 August ; 25(8): 1288–1294. doi:10.1016/j.jvir.2014.03.033.

MRI enables measurement of therapeutic nanoparticle uptake in rat N1-S1 liver tumors after nanoablation

Joseph L. McDevitt, BA[1], **Samdeep Mouli, MD, MS**[1], **Patrick D. Tyler, BA**[1], **Weiguo Li, PhD**[1], **Jodi Nicolai, MS**[1], **Daniele Procissi, PhD**[1], **Ann B. Ragin, PhD**[1], **Y. Andrew Wang, PhD**[2], **Robert J. Lewandowski, MD**[1,3], **Riad Salem, MD, MBA**[1,3], **Andrew C. Larson, PhD**[1,3,4], and **Reed A. Omary, MD, MS**[5]

[1]Department of Radiology, Northwestern University, Chicago, IL

[2]Ocean Nanotech LLC, Springdale, AR

[3]Robert H. Lurie Comprehensive Cancer Center, Northwestern University, Chicago, IL

[4]Department of Biomedical Engineering, Northwestern University, Evanston, IL

[5]Department of Radiology and Radiological Sciences, Vanderbilt University

Abstract

Purpose—Superparamagnetic iron oxide nanoparticles (SPIOs) functionalized with doxorubicin (DOX) can serve dual diagnostic and therapeutic purposes. Nanoablation is an approach to increase intratumoral nanoparticle uptake that combines IV nanoparticle delivery with reversible electroporation. However, a method to quantify drug delivery during this therapy is needed. This study tested the hypothesis that MRI can quantify intratumoral SPIO uptake after nanoablation.

Methods—DOX-SPIOs were synthesized. N1-S1 hepatomas were successfully induced in 17 Sprague-Dawley rats distributed into three dosage groups. Baseline tumor R2* values (the reciprocal of T2*) were determined using 7T MRI. Following IV injection of SPIOs, reversible electroporation (1300 V/cm, 8 pulses, 100 μs pulse duration) was applied. Animals were imaged to determine post-procedural tumor R2* and change in R2* (ΔR2*) was calculated. Inductively-coupled plasma mass spectrometry was used to determine post-procedure intratumoral iron concentration, which served as a proxy for SPIO uptake. Mean tumor iron concentration and ΔR2* for each subject were assessed for correlation with linear regression, and mean iron concentration for each dosage group was compared with analysis of variance.

Corresponding Author: Reed A. Omary, MD, MS, Carol D. and Henry P. Pendergrass Professor and Chair, Department of Radiology and Radiological Sciences, Vanderbilt School of Medicine, Nashville, Tennessee 37232, reed.omary@vanderbilt.edu.

Conflicts of interest: none

Financial disclosures: Reed A. Omary and Andrew C. Larson are co-founders of IORAD (Interventional Oncology Research and Development, LLC)

Material presented at 2012 SIR Annual Scientific Meeting (Cope Award Winner)

Results—ΔR2* significantly correlated with tumor SPIO uptake after nanoablation (r=0.50, p=0.039). On average, each 0.1 ms^{-1} increase in R2* corresponded to a 0.1394 mM increase in iron concentration. There was no significant difference in mean SPIO uptake among dosage groups (p=0.57).

Conclusion—Intratumoral SPIO uptake after nanoablation can be successfully quantified non-invasively with 7T MRI. Imaging can thus be used as a method to estimate localized drug delivery after nanoablation.

INTRODUCTION

Current chemotherapeutic regimens are limited by systemic toxicity and the inability to quantify delivery of therapeutic agents to the target tumor. Nanoparticles, defined as particles of size 1–100 nm, are a promising new class of agents that offer several benefits as potential drug delivery vehicles (1, 2). Nanoparticles a) carry a relatively large payload due to their high surface to volume ratio, b) can exploit the enhanced permeability and retention (EPR) effect, and c) can be customized with various moieties to serve dual diagnostic and therapeutic purposes (3–5). However, nanoparticle delivery to target tumors has been limited by rapid clearance of nanoparticles by the reticuloendothelial system, as well as unpredictable vascular barriers due to the heterogeneity of the EPR effect in large or metastatic tumors (6, 7).

Nanoablation, which combines intravenous (IV) nanoparticle delivery with local reversible electroporation, is an innovative method to increase nanoparticle delivery (8). Unlike irreversible electroporation, which utilizes intense electrical pulses to induce cell death through permanent cell membrane defects, reversible electroporation employs a series of electric pulses that transiently increase the permeability of the targeted cells, resulting in selectively increased drug delivery (9–11). Nanoablation differs from microwave ablation and radiofrequency ablation in that it does not induce necrosis through thermal measures (12). It is a versatile therapy with many applications, as it enhances uptake of superparamagnetic iron oxide nanoparticles (SPIOs) in both hepatic and non-hepatic tumors compared to standard IV dosing (8, 13). Additionally, local electroporation can be combined synergistically with selective intra-arterial nanoparticle delivery (8).

SPIOs act as MRI contrast agents, as their superparamagnetic core causes more rapid T1 and T2 relaxation of immediately surrounding tissues (14). Gradient-echo (GRE) sequences designed to measure T2* relaxation, defined as the decay of transverse magnetization, are particularly sensitive to the changes induced by SPIOs (15). In fact, SPIO concentration has been shown to be proportional to the observed change in R2* (ΔR2*), the reciprocal of T2* (14, 16, 17). However, the quantitative nature of the relationship between intratumoral SPIO concentration and ΔR2* after nanoablation must be established to reliably and non-invasively determine the quantity of chemotherapy delivered to the tumor with this therapy. Thus, we tested the hypothesis that MRI can be used to quantitatively predict intratumoral uptake of therapeutic nanoparticles after nanoablation.

METHODS

Animal Model

All experiments were approved by the Institutional Animal Care and Use Committee. Eighteen male Sprague-Dawley rats (Charles River, Wilmington, MA) weighing 250–380 g underwent tumor implantation, all of which received a standard laboratory diet with free access to water. The N1-S1 rat hepatoma cell line (ATCC, Manassas, VA) was obtained and cultured in Dulbecco's Modified Eagle's Medium (DMEM) (ATCC, Manassas, VA) supplemented with 10% fetal bovine serum (Sigma-Aldrich, St. Louis, MO) and 1% penicillin streptomycin (Invitrogen, Carlsbad, CA). Cells were maintained in suspension culture flasks at 37°C in a humidified atmosphere containing 5% CO_2. Trypan blue staining was performed before each tumor implantation procedure to verify >90% cell viability. The N1-S1 hepatomas were implanted in the left lateral lobe of the liver and grown for 7–10 days according to a published protocol (18).

Therapeutic Agent and Dosage Groups

Iron Oxide (IO) nanoparticles were prepared using iron oxide micropowder as the iron precursor, oleic acid as the ligand, and octadecene as the solvent, as described previously (19). The core and hydrodynamic sizes of the IO nanoparticles were measured using transmission electron microscopy (TEM) and light scattering scan, respectively. IO nanoparticles with 10 nm core size were used for this study. The particles were coated with amphiphilic polymers reported previously, which stabilize IO nanoparticles in water and provide reactive carboxyl groups on the particle surface for bioconjugation (20). To reduce nonspecific binding and uptake by cells, PEG-diamine (molecular weight of 2000) was conjugated to IO nanoparticles by the ethyl-3-dimethyl amino propyl carbodiimide (EDAC) coupling method. PEG-diamine was chosen instead of PEG-monoamino as it should better neutralize the SPIO charge and permit uptake.

Doxorubicin HCl (DOX) in 0.15 M NaCl at 0.5 mg/mL was added to the 10 nm IO particles and vortexed for 1 hour at room temperature. The DOX was attached to the IO core via a pH-labile bond, allowing it to selectively release the DOX in the endosomes and lysosomes of tumor cells following uptake as shown previously (21, 22). The free DOX molecules were separated twice from the encapsulated DOX-SPIOs by a magnetic separator (SuperMag Separator, Ocean NanoTech, Springdale, AR). The DOX loading amount was 20% (w/w Fe) calculated by free DOX left from the supernatant. These DOX-SPIOs were dissolved in deionized water and employed at a concentration of 4 mg/ml Fe.

DOX-SPIO dosages of 0.25 mg/kg, 0.5 mg/kg, and 0.75 mg/kg were employed for the three treatment groups (6 animals each in the 0.25 mg/kg and 0.50 mg/kg groups and 5 animals in the 0.75 mg/kg group). These dosages were chosen to approximate clinically relevant doxorubicin concentrations from previous chemoembolization studies (23–25) and to be consistent with previous animal work on nanoablation (8), while attempting to create a range of concentrations for correlation analysis and to investigate a possible dose-response relationship.

Magnetic Resonance Imaging

A Bruker 7T ClinScan MRI horizontal bore scanner (Bruker, Billerica, MA) with a custom-built rodent receiver coil (Chenguang Med. Tech. Co., Shanghai, China) was employed for all scans. A mixture of 2–5% isoflurane and 2L/min oxygen were supplied via facemask to the subjects during pre-procedural imaging. A small animal monitoring system (SA Instruments, Stony Brook, NY) was used to ensure appropriate sedation and monitor physiologic parameters. Localizer and T2-weighted anatomical scans were performed to verify animal positioning and tumor presence. T2* measurements were obtained before and after nanoablation using the following scan parameters: relaxation time: 700 ms; echo times: 2.56 ms, 6.80 ms, 10.87 ms, 14.59 ms; in-plane field of view (FOV): 7 cm × 7 cm; matrix: 256 × 256; slice thickness: 1.1 mm; flip angle: 30°.

Treatment

MRI was performed 7–10 days after tumor implantation to confirm tumor growth. Tumor size was quantified by maximum diameter in accordance with Response Evaluation Criteria in Solid Tumors (RECIST) guidelines (26). After removal from the MRI scanner, nanoablation was performed as follows: a mini-laparotomy exposed the left lateral lobe of the liver and the femoral vein was catheterized, as in Figure 1. DOX-SPIOs were then injected into the femoral vein. Two minutes after DOX-SPIO injection, electroporation was applied to the tumor via a two-pronged electroporation tool (BTX, Holliston, MA) with two 0.4 mm-diameter needles separated by 1 cm, a configuration which has been shown to provide full coverage of the area between the electrodes (27). Eight 1300 V/cm pulses of 100 μs each with 100 ms between pulses were delivered with an ECM830 function generator (BTX, Holliston, MA) in accordance with previous work (8). The liver was then returned to the abdominal cavity, and the incision was closed via suture. Ten minutes after nanoablation, the subjects were euthanized using pentobarbital (Euthasol ®, Virbac Animal Health, Fort Worth, TX) and immediately returned to the MRI scanner for post-treatment imaging. This necropsy time was chosen because these nanoparticles are known to have rapid first-pass metabolism by reticuloendothelial cells in the liver and spleen and will thus reach steady-state concentration quickly, making long survival unnecessary to study drug delivery (6).

Image Analysis

Quantitative MRI image analysis was performed using ImageJ (NIH, Bethesda, MD). For each tumor, regions-of-interest (ROIs) were drawn in the four largest sections of each tumor in pre- and post-treatment images. For each ROI, the average signal intensity at each of the echo times was determined, and the T2* for each slice was calculated from fitting the intensity/time plot with the following equation: $[\text{Intensity}(t) = Ae^{-t/T2^*}]$. T2* was converted to R2*=1/T2*. The average R2* was determined by a weighted average of the four slices, with weighting by slice area. The ΔR2* that occurred with treatment was calculated by subtracting the pre-treatment R2* from the post-treatment R2*. The volume of each tumor was calculated by multiplying the sum of the cross-sectional areas of all tumor slices by the slice thickness.

Necropsy and Tissue Analysis

Necropsy was performed 1 hour after euthanization and the entire tumor was dissected from the surrounding hepatic parenchyma with a forceps and micro-scissors. Tumor samples were dissolved in 800 μL trace metal grade (70%) nitric acid and filtered with 0.45 μm PTFE syringe filters. 20 μl of filtered, digested sample was transferred to 15 ml metal-free tubes, which was diluted to 2–3% acid with 12 ml of laboratory grade water before the addition of an yttrium internal standard. Iron concentration was then determined via inductively coupled plasma mass spectrometry (ICP-MS) performed on a Thermo XSeries II ICP-MS (Thermo-Fisher, Waltham, MA). This returned the sample iron concentration (in parts per billion) which was converted to the intratumoral iron concentration (in millimoles) using the molecular weight of iron, the tumor volumes calculated as described above, and the fact that for dilute solutions, ppb can be equated to μg/L. The following formula was used for conversions: μg Fe/mL tissue = (“x” μg Fe/1000mL ICPMS soln)*(12 mL ICPMS soln/ 20μL digested soln) *(900 μL digested soln/“y” mL tumor tissue) * (1 mmol Fe/55.85E3 μg Fe).

Statistical Analysis

Statistical analysis was performed using SPSS 21 (IBM, Armonk, NY). Kolmogorov-Smirnov (with p=0.05) and Shapiro-Wilk tests were used to confirm the normal distribution of ΔR2* and [Fe], as well as to confirm the normal distribution of residuals from regression analysis. Mahalanobis Distance (with any value with a Mahalanobis Distance >13.82 defined as significant) was calculated to ensure that there were no outliers or influential points in the regression. A Pearson correlation coefficient (r) was calculated to test the hypothesis that the ΔR2* that occurred with treatment linearly predicted the post-treatment intratumoral iron concentration, with $p<0.05$ considered significant. The following equation was used: $Fe_1 = Fe_0 + r^*(R2^*_1 – R2^*_0)$, where $R2^*_0$ is the pre-treatment R2*, $R2^*_1$ is the post-treatment R2*, Fe_1 is the post-treatment intratumoral iron concentration, Fe_0 is the estimated average pre-treatment intratumoral iron concentration, and r* is the estimated relativity of these DOX-SPIOs, measured in mM^*ms^{-1}. The means of the three treatment groups were compared using one-way analysis of variance (ANOVA) with $p<0.05$ considered significant.

RESULTS

N1-S1 Tumors were successfully grown in 17 of the 18 Sprague-Dawley rats in which they were implanted (implantation rate=94%), with median diameter of 0.75 cm (range 0.35–0.95 cm) and median volume of 0.30 mL (range 0.027–0.680 mL).

Uptake of DOX-SPIOs into the tumors, hepatic parenchyma, and spleen was detected qualitatively by MRI, with reductions in T2* within the tumor, liver, and spleen of each treated animal (Figures 2 and 3). Mean post-treatment intratumoral iron concentration ([Fe]) was 1.61 mM (range 0.34–2.99 mM), and mean ΔR2* was 0.04 ms^{-1} (range 0.002–0.12 ms^{-1}). Mean [Fe] by dosage group is provided in Table 1 and represented graphically in Figure 4. There was no statistically significant difference among the mean intratumoral [Fe] in the three dosage groups (F=0.57, P=0.58).

A significant positive correlation was observed between the change in tumor R2* (ΔR2*) and the post-treatment intratumoral [Fe] ($r=0.50$, $p=0.039$, $SE_{correlation}=0.22$). A linear equation was generated that quantitatively predicted millimolar post-treatment intratumoral [Fe] (a proxy for nanoparticle uptake) as a function of R2*: $[Fe]= 1.00 + 13.94\times\Delta R2^*$(Figure 5). The slope of this regression line (13.94 mM^*ms^{-1}) is the relaxivity of DOX-SPIOs in the rat N1-S1 hepatoma.

DISCUSSION

This study demonstrates proof of the concept that 7T MRI can successfully quantify SPIO delivery to liver tumors after nanoablation in a rat model. Given this information, along with the established stability of the doxorubicin conjugated to these SPIOs and knowledge of the DOX/SPIO binding ratio, the amount of DOX delivered to the tumor can be estimated from imaging data. More broadly, this suggests that MRI can be used to non-invasively measure the uptake of chemotherapeutic drugs conjugated to nanoparticles.

MRI has been used to image nanoparticle distribution in a variety of contexts, such as neuroinflammation in root compression (28), soft tissue infection (29), atherosclerosis (30, 31), and angiogenesis in tumor models (32, 33), as well as to confirm SPIO delivery to rabbit liver tumors (8, 34). Recent work in a different rodent model of HCC showed that MRI can quantify both intratumoral uptake of SPIOs after intravenous delivery (17) and labeled NK cells after intra-arterial delivery (35). Additionally, treatment groups with increased SPIO delivery have a greater mean $R2^*_{post}$ (8). However, it was unclear if there was a linear relationship between the uptake of chemotherapeutic nanoparticles after nanoablation and ΔR2* at the level of the individual animal. Our current study addresses this unmet gap in knowledge by showing that MRI can be used to predict the intratumoral uptake of DOX-SPIOs for individual tumors, even in the presence of electroporation.

Estimation of on- and off-target delivery with local therapies is challenging. In chemoembolization, the patient's underlying arterial anatomy and the success of selective catheterization determine the success of the treatment, rather than the total delivered systemic dose (36). Additionally, plasma doxorubicin levels after chemoembolization, though significant, are highly variable and bear no relation to injected dose (37). The results of our study are consistent with these findings, as there was no relationship between injected dose and mean intratumoral iron concentration. Taken together, these findings suggest that the efficacy of local drug delivery depends primarily upon local tumor factors that could be modified by a therapy such as electroporation, rather than the systemically delivered dose. Such information only makes the ability to measure the efficacy of local drug delivery more critical.

This study offers several potential benefits. First, our imaging approach could assist in the design of future studies that aim to measure intratumoral concentrations of locally delivered agents. Current factors used to determine systemic dosing, such as weight and body surface area, would be expected to have little bearing on such trials. These studies would have the goal of establishing the smallest effective intratumoral dose, potentially reducing systemic and hepatic toxicity. Second, intratumoral drug concentrations may correlate with clinical

outcomes, and could serve as a surrogate endpoint for therapy. Thus, physicians could avoid the need to wait weeks to months to ascertain post-procedural response using conventional anatomic imaging changes of tumor size or necrosis (38).

This study is similar in design to that of Tyler et al (17), with the addition of tissue manipulation in the form of laparotomy and reversible electroporation. This additional manipulation made matching the planes of pre- and post-procedure MR slices more challenging. The increased difficulty of image co-registration is reflected in the lower R value in comparison to the previous study. Thus, although we have demonstrated that SPIOs can be quantified even after a locally invasive procedure, further technical refinements that allow for easier co-registration, such as percutaneously delivered electroporation, will likely further improve the predictive power of MRI.

This study has several important limitations. First, the long-term biodistribution of injected SPIOs was not characterized, and the efficacy of nanoablation was not assessed. These outcome measures are now appropriate subjects for a follow-up study. Second, intratumoral doxorubicin concentration could not be directly measured. Instead, we chose to use the entire tumor specimen for ICP-MS analysis, as this provided the most accurate gold standard for the measurement of iron concentrations. Third, the study was performed in one model of human HCC, the rat N1-S1 tumor model, which has histologic similarity to human HCC, but it is not as hypervascular as human HCC (39). Although the vascularity difference should lead to a lower concentration of nanoparticles delivered to N1-S1 tumors relative to human HCC, this difference should have no effect on the correlation between ΔR2* and intratumoral iron concentration. Fourth, the tumors employed in this study had a range of diameters. Although previous research has shown that the treatment zones induced by the employed electroporation technique will fully cover the treated tumors (27), future investigators could explore if tumors of different size have differential responses to electroporation, and thus differential uptake properties based upon their distance from the electroporation electrodes. Finally, recent work showed that N1-S1 tumors spontaneously regress within 5 weeks of implantation, making the N1-S1 unsuitable for long-term survival studies (40). However, the N1-S1 model still remains a valid model to study drug uptake and delivery.

There are several future studies that could enhance this line of research. The correlation between ΔR2*and [Fe] in the liver and spleen should be investigated, as reliably quantifying off-target delivery will be important to predict systemic toxicity. Also, future studies that directly compare SPIO uptake and doxorubicin concentration could further validate the model's predictive accuracy. A similar study should also be completed investigating the predictive value of MR with intra-arterial delivery in a larger animal model, which is more similar to chemoembolization. Also, although this study showed the predictive value of 7T MRI, clinical translation would require validation at 1.5T or 3T field strengths.

In conclusion, this study demonstrated proof of the concept that MRI can be used to quantitatively predict the delivery of therapeutic nanoparticles after nanoablation. This knowledge might be used in the future to help improve therapies by a) providing immediate

feedback on procedural efficacy and b) determining dosing paradigms for nanoparticle therapies.

Acknowledgments

Rachel Klein, BS

REFERENCES

1. Davis ME, Chen Z, Shin DM. Nanoparticle therapeutics: an emerging treatment modality for cancer. Nat Rev Drug Discov. 2008; 7:771–782. [PubMed: 18758474]
2. Nie S. Understanding and overcoming major barriers in cancer nanomedicine. Nanomedicine (Lond). 2010; 5:523–528. [PubMed: 20528447]
3. Peng X-H, Quian X, Mao H, et al. Targeted magnetic iron oxide nanoparticles for tumor imaging and therapy. Int J Nanomedicine. 2010; 3:311–321. [PubMed: 18990940]
4. Sun C, Lee J, Zhang M. Magnetic nanoparticles in MR imaging and drug delivery. Adv Drug Deliv Rev. 2008; 60:1252–1265. [PubMed: 18558452]
5. Desai N. Challenges in the development of nanotherapeutics. AAPS J. 2012; 14:282–295. [PubMed: 22407288]
6. Cho K, Wang X, Nie S. Therapeutic nanoparticles for drug delivery in cancer. Clin Cancer Res. 2008; 14:1310–1316. [PubMed: 18316549]
7. Fang J, Nakamura H, Maeda H. The EPR effect: unique features of tumor blood vessels for drug delivery, factors involved, and limitations and augmentation of the effect. Adv Drug Deliv Rev. 2011; 63:136–151. [PubMed: 20441782]
8. Mouli SK, Tyler P, McDevitt JL, et al. Image-guided local delivery strategies enhance therapeutic nanoparticle uptake in solid tumors. ACS Nano. 2013; 7:7724–7733. [PubMed: 23952712]
9. Sersa G, Cemazar M, Snoj M. Electrochemotherapy of tumours. Curr Oncol. 2009; 16:34–35. [PubMed: 19370177]
10. Mir LM, Orlowski S. Mechanisms of electrochemotherapy. Adv Drug Deliv Rev. 1999; 35:107–118. [PubMed: 10837692]
11. Guo Y, Zhang Y, Klein R, et al. Irreversible electroporation therapy in the liver: longitudinal efficacy studies in a rat model of hepatocellular carcinoma. Cancer Res. 2010; 70:1555–1563. [PubMed: 20124486]
12. Lencioni R, Crocetti L, De Simone P, Filipponi F. Loco-regional interventional treatment of hepatocellular carcinoma: techniques, outcomes, and future prospects. Transplant Int. 2010; 23:698–703.
13. Eifler AC, Lewandowski RJ, Mouli S, et al. Abstract No. 70 [Cope]: Image-guided nanoembolization as a novel local therapy for pancreatic cancer: feasibility in an animal model. J Vasc Interv Radiol. 2010; 21:S28.
14. Winkelmann S, Schaeffter T, Weiss S, Eggers H, Doessel O. Simultaneous imaging and R2* mapping using a radial multi-gradient-echo (rMGE) sequence. J Magn Reson Imaging. 2006; 24:939–944. [PubMed: 16958064]
15. Chavhan GB, Babyn PS, Thomas B, Shroff MM, Haacke EM. Principles, techniques, and applications of T2*-based MR imaging and its special applications. RadioGraphics. 2009; 29:1433–1449. [PubMed: 19755604]
16. Yablonskiy D, Haacke E. Theory of NMR signal behavior in magnetically inhomogenous tissues: the static dephasing regime. Magn Reson Med. 1994; 32:749–763. [PubMed: 7869897]
17. Tyler PD, McDevitt JL, Sheu AY, et al. Seven-tesla magnetic resonance imaging accurately quantifies intratumoral uptake of therapeutic nanoparticles in the McA rat model of hepatocellular carcinoma: preclinical study in a rodent model. Invest Radiol. 2014; 49:87–92. [PubMed: 24089022]

18. Garin E, Denizot B, Roux J, et al. Description and technical pitfalls of a hepatoma model and of intra-arterial injection of radiolabelled lipiodol in the rat. Lab Anim. 2005; 39:314–320. [PubMed: 16004691]
19. Yu WW, Falkner JC, Yavuz CT, Colvin VL. Synthesis of monodisperse iron oxide nanocrystals by thermal decomposition of iron carboxylate salts. Chem Commun (Camb). 2004; 20:2306–2307. [PubMed: 15489993]
20. Duan H, Kuang M, Wang X, et al. Reexamining the effects of particle size and surface chemistry on the magnetic properties of iron oxide nanocrystals: new insights into spin disorder and proton relaxivity. J Phys Chem C. 2008; 112:8127–8131.
21. Yang L, Cao Z, Sajja HK, et al. Development of receptor targeted magnetic iron oxide nanoparticles for efficient drug delivery and tumor imaging. J Biomed Nanotechnol. 2008; 4:439–449.
22. Maeng JH, Lee D-H, Jung KH, et al. Multifunctional doxorubicin loaded superparamagnetic iron oxide nanoparticles for chemotherapy and magnetic resonance imaging in liver cancer. Biomaterials. 2010; 31:4995–5006. [PubMed: 20347138]
23. Lewandowski RJ, Mulcahy MF, Kulik LM, et al. Chemoembolization for hepatocellular carcinoma: comprehensive imaging and survival analysis in a 172-patient cohort. Radiology. 2010; 255:955–965. [PubMed: 20501733]
24. Solomon B, Soulen MC, Baum RA, et al. Chemoembolization of hepatocellular carcinoma with cisplatin, doxorubicin, mitomycin-C, ethiodol, and polyvinyl alcohol: prospective evaluation of response and survival in a U.S. population. J Vasc Interv Radiol. 1999; 10:793–798. [PubMed: 10392950]
25. Ramsey DE, Kernagis LY, Soulen MC, Geschwind J-FH. Chemoembolization of hepatocellular carcinoma. J Vasc Interv Radiol. 2002; 13:S211–S221. [PubMed: 12354839]
26. Therasse P, Eisenhauer EA, Verweij J. RECIST revisited: a review of validation studies on tumour assessment. Eur J Cancer. 2006; 42:1031–1039. [PubMed: 16616487]
27. Faroja M, Ahmed M, Appelbaum L, et al. Irreversible electroporation ablation: is all the damage nonthermal? Radiology. 2013; 266:462–470. [PubMed: 23169795]
28. Thorek DLJ, Weisshaar CL, Czupryna JC, Winkelstein BA, Tsourkas A. Superparamagnetic iron oxide-enhanced magnetic resonance imaging of neuroinflammation in a rat model of radicular pain. Mol Imaging. 2011; 10:206–214. [PubMed: 21496449]
29. Lutz AM, Weishaupt D, Persohn E, et al. Imaging of macrophages in soft-tissue infection in rats: relationship between ultrasmall superparamagnetic iron oxide dose and MR signal characteristics. Radiology. 2005; 234:765–775. [PubMed: 15665219]
30. Tsourkas A, Shinde-Patil VR, Kelly KA, et al. In vivo imaging of activated endothelium using an anti-VCAM-1 magnetooptical probe. Bioconjug Chem. 2005; 16:576–581. [PubMed: 15898724]
31. Sigovan M, Kaye E, Lancelot E, et al. Anti-inflammatory drug evaluation in ApoE−/− mice by ultrasmall superparamagnetic iron oxide–enhanced magnetic resonance imaging. Invest Radiol. 2012; 47:546–552. [PubMed: 22864378]
32. Bremer C, Mustafa M, Bogdanov A, et al. Steady-state blood volume measurements in experimental tumors with different angiogenic burdens—a study in mice. Radiology. 2003; 226:214–220. [PubMed: 12511693]
33. Cho E-J, Yang J, Mohamedali KA, et al. Sensitive angiogenesis imaging of orthotopic bladder tumors in mice using a selective magnetic resonance imaging contrast agent containing VEGF121/rGel. Invest Radiol. 2011; 46:441–449. [PubMed: 21512397]
34. Lee K-H, Liapi E, Vossen JA, et al. Distribution of iron oxide–containing embosphere particles after transcatheter arterial embolization in an animal model of liver cancer: evaluation with MR imaging and implication for therapy. J Vasc Interv Radiol. 2008; 19:1490–1496. [PubMed: 18755602]
35. Sheu AY, Zhang Z, Omary RA, Larson AC. MRI-monitored transcatheter intra-arterial delivery of SPIO-labeled natural killer cells to hepatocellular carcinoma: preclinical studies in a rodent model. Invest Radiol. 2013; 48:492–499. [PubMed: 23249649]

36. Lewandowski RJ, Tepper J, Wang D, et al. MR imaging perfusion mismatch: a technique to verify successful targeting of liver tumors during transcatheter arterial chemoembolization. J Vasc Interv Radiol. 2008; 19:698–705. [PubMed: 18440458]

37. Varela M, Real MI, Burrel M, et al. Chemoembolization of hepatocellular carcinoma with drug eluting beads: efficacy and doxorubicin pharmacokinetics. J Hepatol. 2007; 46:474–481. [PubMed: 17239480]

38. Smith K, Kim H. Interventional radiology and image-guided medicine. Semin Oncol. 2011; 38:151–162. [PubMed: 21362523]

39. Guo Y, Klein R, Omary RA, Yang G-Y, Larson AC. Highly malignant intra-hepatic metastatic hepatocellular carcinoma. Am J Transl Res. 2011; 3:114–120. [PubMed: 21139811]

40. Buijs M, Geschwind J-FH, Syed LH, et al. Spontaneous tumor regression in a syngeneic rat model of liver cancer: implications for survival studies. J Vasc Interv Radiol. 2012; 23:1685–1691. [PubMed: 23177115]

Figure 1.
Representative subject configuration prior to nanoablation.

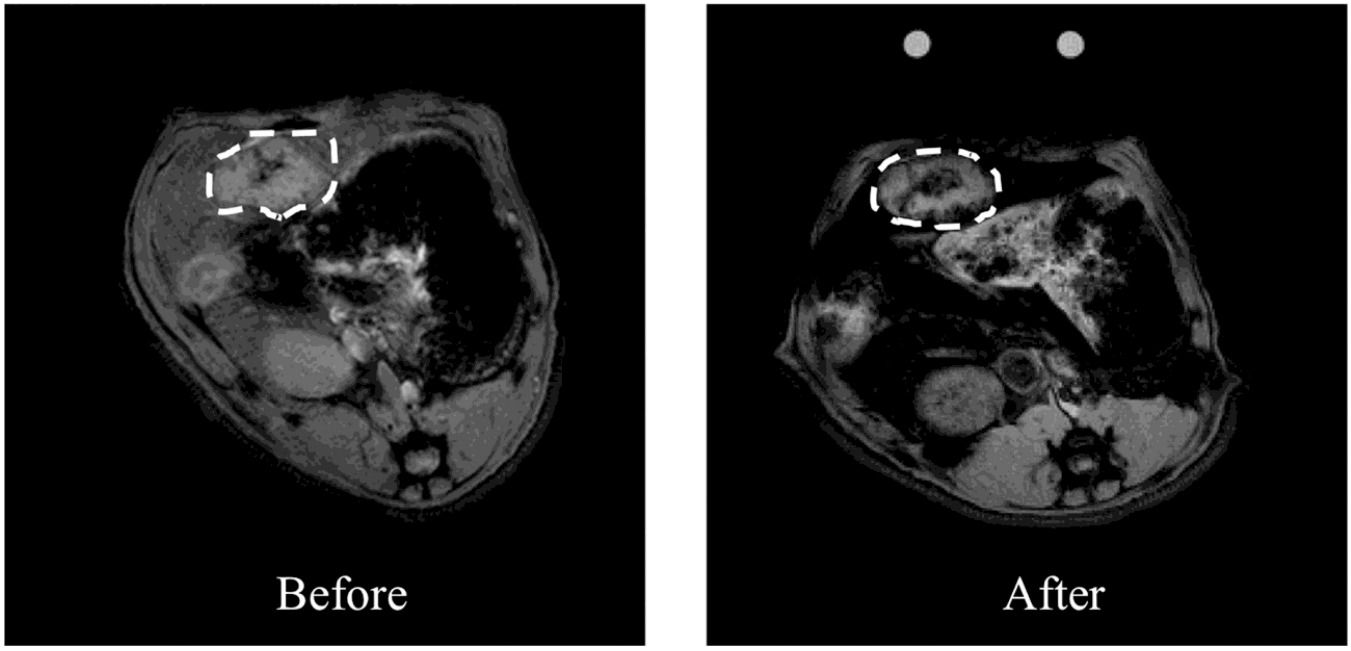

Figure 2.

Representative axial MR images of N1-S1 rat hepatoma obtained at 7T before and after nanoablation. Brightness corresponds to the raw measured intensity at the first echo time (t=2.56 ms). SPIO uptake can be visualized on the raw intensity scans by diminished brightness in the tumor (as denoted by dashed lines) and surrounding liver in the post-treatment image relative to the pre-treatment image.

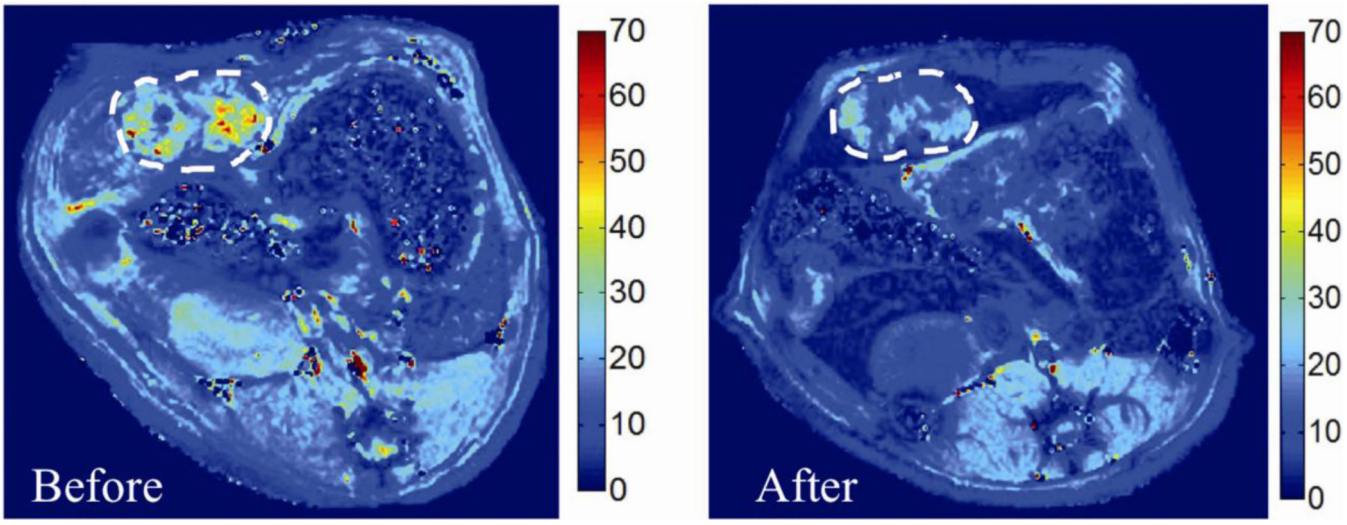

Figure 3.

Representative axial MR images of N1-S1 rat hepatoma obtained at 7T before and after nanoablation, in which the color scale corresponds to the T2* value in miliseconds (ms). SPIO uptake can be visualized by diminished color intensity (measured in ms) in the tumor (as denoted by dashed lines) and surrounding liver in the post-treatment image relative to the pre-treatment image.

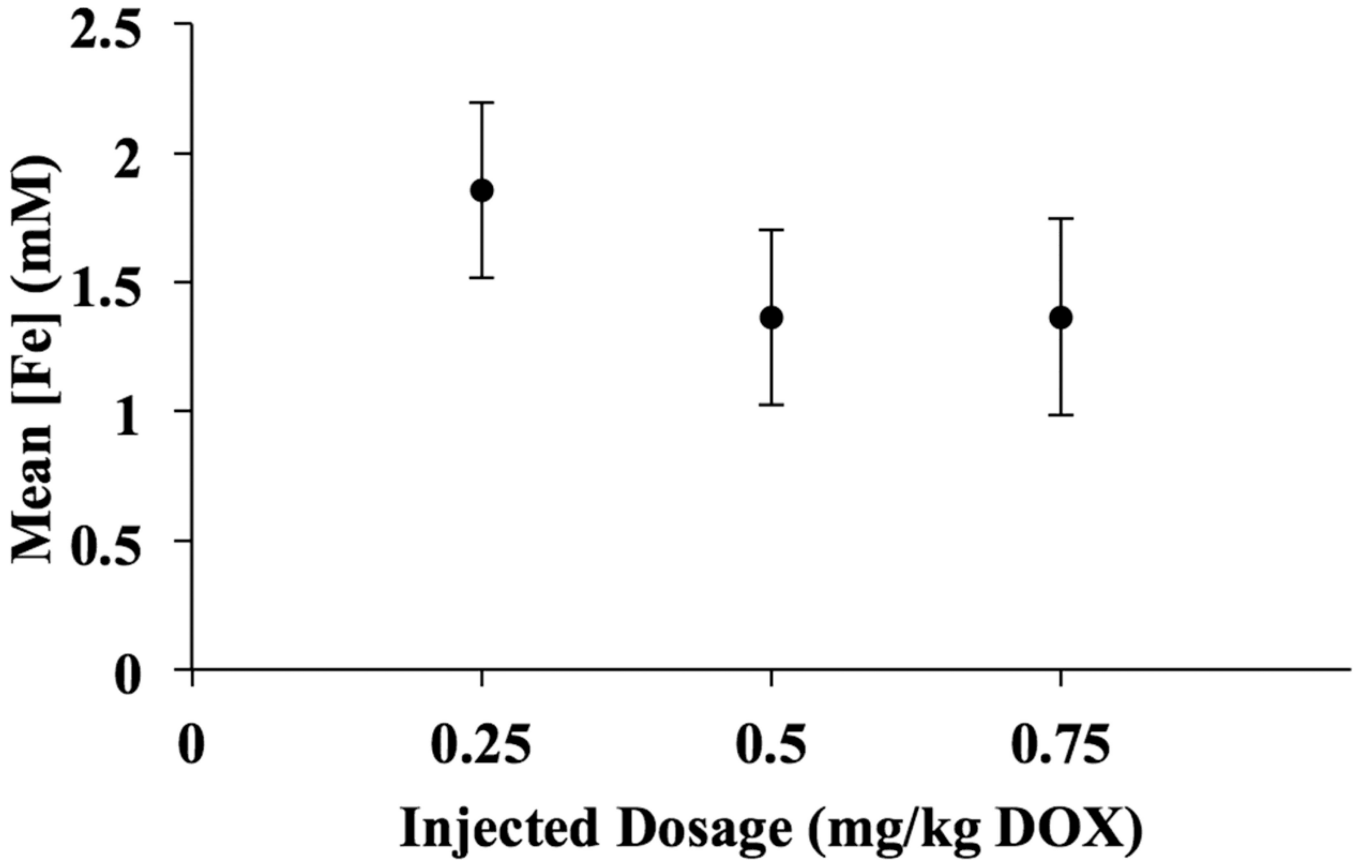

Figure 4.
Average post-procedural intratumoral iron concentration by dosage group (mg/kg DOX-SPIOs). Error bars represent standard error of the mean (mM).

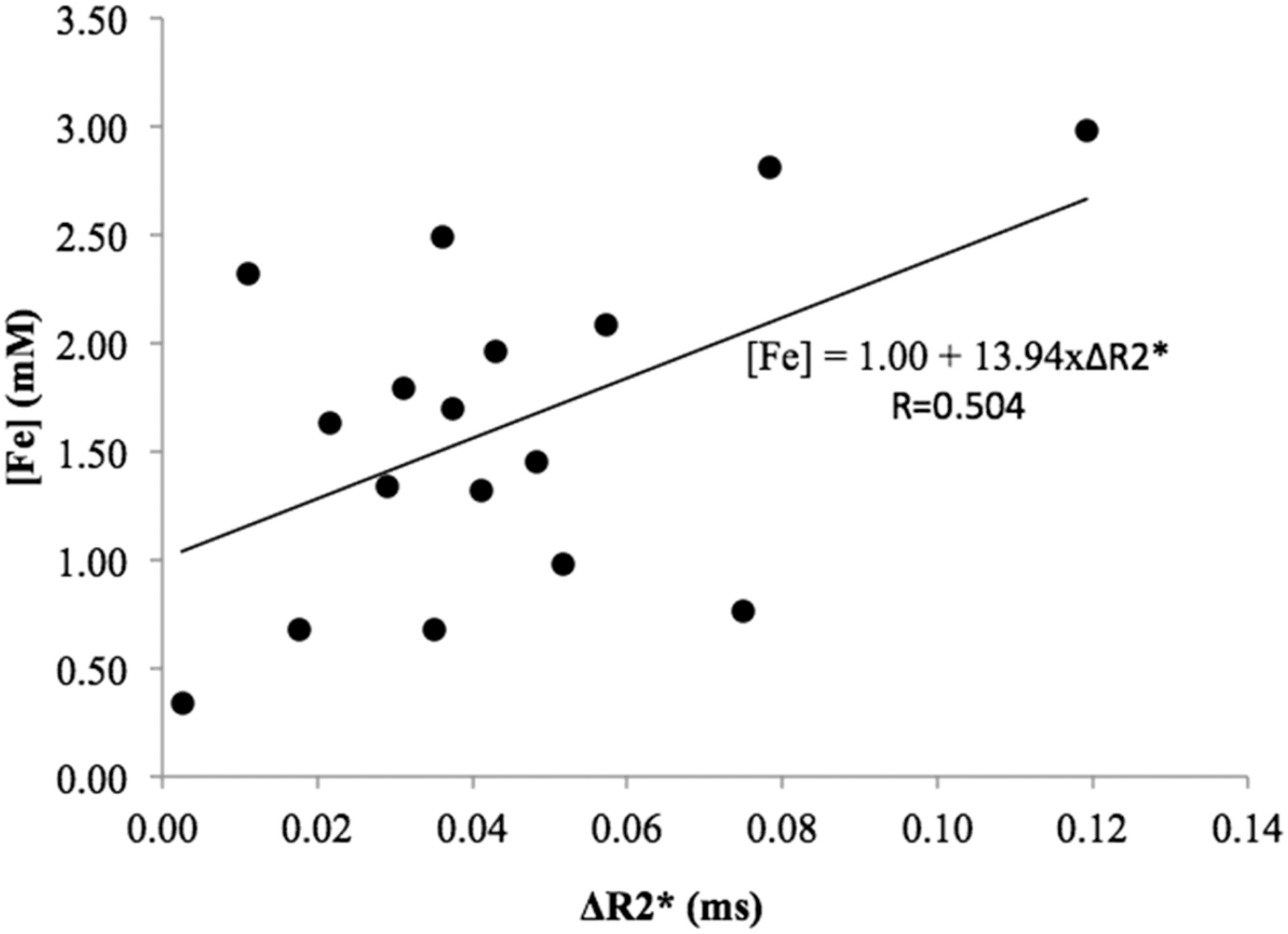

Figure 5.

Individual ΔR2* plotted against corresponding final intratumoral iron concentration. The slope of the regression line represents the linear relationship between mean ΔR2* and intratumoral SPIO uptake, which is equal to the relaxivity.

Table 1

Mean intratumoral iron concentration and standard deviation for each treatment group.

Dosage Group (mg/kg DOX)	Mean Tumor [Fe] (mM)	Standard Deviation (mM)
0.25	1.86	0.84
0.50	1.36	0.85
0.75	1.60	0.66